Engineering Analysis with Boundary Elements 33 (2009) 561–571

Contents lists available at ScienceDirect

Engineering Analysis with Boundary Elements

journal homepage: www.elsevier.com/locate/enganabound

BEM simulation of compressible fluid flow in an enclosure induced by thermoacoustic waves

L. Škerget *, J. Ravnik

Faculty of Mechanical Engineering, University of Maribor, Smetanova 17, SI-2000 Maribor, Slovenia

ARTICLE INFO

Article history:
Received 21 January 2008
Accepted 12 August 2008
Available online 20 September 2008

Keywords:
Compressible fluid flow
Boundary element method
Thermoacoustic waves
Velocity-vorticity formulation

ABSTRACT

The problem of unsteady compressible fluid flow in an enclosure induced by thermoacoustic waves is studied numerically. Full compressible set of Navier–Stokes equations are considered and numerically solved by boundary-domain integral equations approach coupled with wavelet compression and domain decomposition to achieve numerical efficiency. The thermal energy equation is written in its most general form including the Rayleigh and reversible expansion rate terms. Both, the classical Fourier heat flux model and wave heat conduction model are investigated.

The velocity–vorticity formulation of the governing Navier–Stokes equations is employed, while the pressure field is evaluated from the corresponding pressure Poisson equation. Material properties are taken to be for the perfect gas, and assumed to be pressure and temperature dependent.

1. Introduction

In the paper the generation and transmission of thermoacoustic waves in an perfect gas filled closed cavity is studied numerically. When a compressible fluid is subjected to a rapid increase in temperature at a solid wall, a sudden expansion of the adjacent gas occurs. This phenomenon generates a fast increase in the local pressure and leads to the production of pressure waves. These thermally generated waves are referred to as thermoacoustic waves.

During the expansion phase, the wave temperature dips below the average medium temperature. The thermoacoustic waves propagate at approximately the speed of sound within the fluid and gradually damp out due to heat and momentum diffusion.

Thermoacoustic transport phenomena may be very interesting, when the fluid is close to thermodynamic critical point or when other modes of transport mechanism are weak or absent. Thermoacoustic waves enhance heat transport by converting the thermal energy into compression work and by inducing convection motion away from the heated wall. This mode of heat transfer is dominant in the space environment under zero- or reduced-gravity conditions, where natural convection of heat transport may be absent or low, and when heat conduction is the only mode of heat transport mechanism.

The problem of thermoacoustic transport phenomena in a perfect gas confined in an enclosure subjected to a sudden increase in temperature at a solid wall have been considered experimentally and numerically by Huang and Bau [1,2] as well as by Brown and Churchill [3]. In the literature one can find analytical attempts to study the phenomenon limited mainly to simplified models, while the solutions to general cases have been performed by numerical approximative methods. In the present paper the boundary element method (BEM) is used. Previous studies of Lin and Farouk [4], Aktas and Farouk [5], Farouk et al. [6], Škerget and Ravnik [7], observed strong thermoacoustic waves as a consequence of impulsive heating. Horizontal velocity component reverses sign after reflection from the side walls. The flow field is essentially one-dimensional.

We examine the thermal energy equation for a flow which is neither constant density nor constant pressure. Here we consider the unsteadiness of compressible viscous flow of perfect gas in an enclosure due to thermoacoustic waves. The thermal energy equation is written in its most expanded form with the terms such as the rate of reversible work and the rate of irreversible or dissipation work. The coupled momentum, thermal energy transport and pressure equations, specially due to mentioned rate of work terms, drastically increased the nonlinearity of the governing set of equations, and as a consequence decreased the stability of the numerical algorithm.

The unsteadiness of the thermoacoustic waves are considered in a square enclosure with side length $L = 0.013$ m under zero- or normal-gravity conditions. The classical Fourier heat conduction model, based on an infinite thermal propagation speed, gives realistic approximations for most practical engineering heat transfer applications. However, this model is no longer applicable

* Corresponding author. Tel.: +386 38662 25461.
E-mail addresses: leo@uni-mb.si (L. Škerget), jure.ravnik@uni-mb.si (J. Ravnik).

0955-7997/$ - see front matter © 2008 Elsevier Ltd. All rights reserved.
doi:10.1016/j.enganabound.2008.08.003

for intensive transient or periodic heat transfer phenomena, when the finite thermal propagation speed is important for thermal analysis. The influence of wave heat conduction model is investigated. The non-Fourier effect is significant for a short time after the initial transient depending on a thermal relaxation time.

In this research we simulate laminar viscous Newtonian flow using the velocity–vorticity formulation of the compressible Navier–Stokes equations [8–12]. In the velocity–vorticity formulation the pressure is eliminated from the system and replaced by the vorticity. The accurate calculation of boundary vorticity values is of utmost importance, since the vorticity is generated at the boundary. The solution of the transport equation only carries the vorticity, generated at the boundary, into the flow with diffusion and advection. Other authors proposed several different schemes for the calculation of boundary vorticity [13,14]. We propose to use BEM [15] because of its unique advantage for solving the boundary vorticity values directly.

For the solution of the domain values single domain BEM requires large storage and long CPU times. In order to avoid this difficulty Škerget et al. [16] proposed a subdomain BEM technique, which was used by Ramšak et al. [17] and Ravnik et al. [18,19]. Hriberšek et al. [20] developed a segmentation technique. Žunič et al. [21] proposed a combined BEM–finite element method (FEM) algorithm, replacing subdomain BEM by FEM. The algorithm was used to simulate particle laden flows by Ravnik et al. [22]. Other BEM domain decomposition techniques are described in Popov et al. [23].

In order to be able to perform simulations on dense grids, we used a wavelet compression algorithm on fully populated matrices, resulting from the BEM calculation of boundary vorticity, to further decrease the computer memory and CPU time requirements of the coupled BEM–FEM algorithm. A discrete wavelet transform for vectors of arbitrary length, developed by Ravnik et al. [24,25], was used. Ravnik et al. [25] developed a two-dimensional large-eddy simulation code, that was based on the combination of wavelet transform, BEM and FEM. Using a laminar version of this code enabled us to make unsteady simulations on dense grids with small time steps.

2. Governing equations for the primitive variables formulation

The field functions of interest are velocity vector field v_i, scalar pressure field p, temperature field T and the field of mass density ρ, so that the mass, momentum and energy equations are given by the following set of nonlinear equations:

$$\frac{\partial v_j}{\partial x_j} = \mathscr{D} = -\frac{1}{\rho}\frac{\mathrm{D}\rho}{\mathrm{D}t}, \tag{1}$$

$$\rho\frac{\mathrm{D}v_i}{\mathrm{D}t} = -e_{ijk}\frac{\partial \eta\omega_k}{\partial x_j} + 2e_{ijk}\frac{\partial \eta}{\partial x_j}\omega_k + 2\frac{\partial \eta}{\partial x_j}\frac{\partial v_i}{\partial x_j} + \frac{4}{3}\frac{\partial \eta\mathscr{D}}{\partial x_i} - 2\mathscr{D}\frac{\partial \eta}{\partial x_i} - \frac{\partial p}{\partial x_i} + \rho g_i, \tag{2}$$

$$c\frac{\mathrm{D}T}{\mathrm{D}t} = \frac{\partial}{\partial x_j}\left(k\frac{\partial T}{\partial x_j} + \lambda\frac{\partial q_j}{\partial t}\right) + \beta T\frac{\mathrm{D}p}{\mathrm{D}t} + \Phi, \tag{3}$$

in the Cartesian frame x_i, where c denotes changeable isobaric specific heat capacity per unit volume, $c = c_p\rho, t$ is time, g_i is gravitational acceleration vector, while β is a volume coefficient of thermal expansion, λ is a heat relaxation time and Φ is the Rayleigh viscous dissipation function. Because of the analytical reasons required by the derivation of the velocity–vorticity formulation of the governing equations, the momentum equation is given in the second extended form.

The Newton momentum diffusion constitutive model for compressible viscous shear fluid is considered, such as

$$\tau_{ij} = 2\eta\dot{\varepsilon}_{ij} - \tfrac{2}{3}\eta\mathscr{D}\delta_{ij}, \tag{4}$$

where $\mathscr{D} = div\,\vec{v} = \dot{\varepsilon}_{ii}$ represents the divergence of the velocity field or local expansion field, and the Rayleigh dissipation function may be stated as

$$\Phi = \tau_{ij}\frac{\partial v_i}{\partial x_j} = \eta\left(\frac{\partial v_i}{\partial x_j}\frac{\partial v_i}{\partial x_j} + \frac{\partial v_j}{\partial x_i}\frac{\partial v_j}{\partial x_i}\right) - \frac{2}{3}\eta\mathscr{D}^2. \tag{5}$$

In the case of intensive unsteady heat transfer, it is important to take into account a terminal velocity of a moving temperature frontier, namely the following form of heat flux constitutive model:

$$q_i = -k\frac{\partial T}{\partial x_i} - \lambda\frac{\partial q_i}{\partial t}, \tag{6}$$

where material constants k and λ are the heat conductivity and the heat relaxation time. For most heat transfer problems of practical importance, the simplification known as the Fourier law of heat diffusion is accurate enough, namely

$$q_i = -k\frac{\partial T}{\partial x_i}. \tag{7}$$

Representing the material properties of the fluid the dynamic viscosity η, heat conductivity k, the specific heat per unit volume c, and the mass density ρ, are written as sums of a constant and variable part, e.g. $\eta = \eta_0 + \tilde{\eta}, k = k_0 + \tilde{k}, c = c_0 + \tilde{c}$, and $\rho = \rho_0 + \tilde{\rho}$, so the momentum and energy equations (2) and (3) may be written in analogy to the basic conservation equations formulated for the constant material properties

$$\frac{\mathrm{D}\vec{v}}{\mathrm{D}t} = -v_0\vec{\nabla}\times\vec{\omega} - \frac{1}{\rho_0}\vec{\nabla}p + \frac{\rho}{\rho_0}\vec{g} + \frac{1}{\rho_0}\vec{f}^m, \tag{8}$$

$$\frac{\mathrm{D}T}{\mathrm{D}t} = a_0\Delta T + \frac{S^m}{c_0}, \tag{9}$$

where the pseudo-body force term $\vec{f}^m$ and pseudo-heat source term S^m are introduced into the momentum equation (8) and into energy equation (9), respectively, capturing the variable material property effects, and the nonlinear effects due to rate of reversible and irreversible work, and given by expressions, e.g. for plane flow problems

$$f_i^m = -e_{ij}\frac{\partial\tilde{\eta}\omega}{\partial x_j} + 2e_{ij}\frac{\partial\tilde{\eta}}{\partial x_j}\omega + 2\frac{\partial\eta}{\partial x_j}\frac{\partial v_i}{\partial x_j} + \frac{4}{3}\frac{\partial\eta\mathscr{D}}{\partial x_i} - 2\mathscr{D}\frac{\partial\eta}{\partial x_i} - \tilde{\rho}a_i, \tag{10}$$

while the pseudo-heat source term is given by an expression

$$S^m = \vec{\nabla}\left(\tilde{k}\vec{\nabla}T + \lambda\frac{\partial\vec{q}}{\partial t}\right) - \tilde{c}\frac{\mathrm{D}T}{\mathrm{D}t} + \beta T\frac{\mathrm{D}p}{\mathrm{D}t} + \Phi, \tag{11}$$

in which the kinematic viscosity is $v_0 = \eta_0/\rho_0$, the heat diffusivity $a_0 = k_0/c_0$ and the inertia acceleration vector is $\vec{a} = \mathrm{D}\vec{v}/\mathrm{D}t$.

3. Governing equations for the velocity–vorticity formulation

The kinematics of the flow motion may be obtained by applying the curl operator to vorticity definition

$$\vec{\nabla}\times\vec{\omega} = \vec{\nabla}\times(\vec{\nabla}\times\vec{v}) = \vec{\nabla}(\vec{\nabla}\cdot\vec{v}) - \Delta\vec{v}, \tag{12}$$

and by using the continuity equation (1). The following vector elliptic Poisson equation for the velocity vector is derived:

$$\Delta\vec{v} + \vec{\nabla}\times\vec{\omega} - \vec{\nabla}\mathscr{D} = 0. \tag{13}$$

The kinetics of the flow representing the vorticity transport equation is obtained by applying the curl differential operator to

the both sides of Eq. (8), rendering the following statement for the two-dimensional plane flow written in Cartesian tensor notation form as

$$\frac{\partial \omega}{\partial t}+\frac{\partial v_j \omega}{\partial x_j}=\nu_0 \frac{\partial^2 \omega}{\partial x_j \partial x_j}-\frac{1}{\rho_0} e_{ij} \frac{\partial \rho g_i}{\partial x_j}-\frac{1}{\rho_0} e_{ij} \frac{\partial f_i^m}{\partial x_j}. \tag{14}$$

To derive the pressure equation, depending on known velocity field, vorticity field and material functions, the divergence of momentum equation should be calculated, resulting in the elliptic Poisson pressure equation

$$\Delta p-\vec{\nabla}\cdot\vec{f}_p=0, \tag{15}$$

where the pressure force term $\vec{f}_p$ is for the planar flow cases

$$\frac{\partial p}{\partial x_i}=f_{pi}=-\eta_0 e_{ij}\frac{\partial \omega}{\partial x_j}-\rho_0 a_i+\rho g_i+f_i^m. \tag{16}$$

The Neumann boundary conditions for pressure equation may be determined for the whole solution domain and the following relation is valid

$$\frac{\partial p}{\partial n}=\vec{f}_p\cdot\vec{n} \quad \text{on } \Gamma. \tag{17}$$

Due to the variable material property terms, and rate of reversible and irreversible work acting as additional temperature, pressure and velocity field dependent source terms, the vorticity, thermal energy, and pressure equations are coupled, making the numerical solution procedure of this highly nonlinear coupled set of equations very severe. Already, the vorticity transport equation as itself is highly nonlinear partial differential equation due to the inherent nonlinearity caused by the compatibility and restriction conditions among velocity, vorticity and dilatation fields. The dilatation and the vortical part of the flow, $\mathscr{D}$ and $\vec{\omega}$ field functions, respectively, and all other nonlinear terms have to be under-relaxed to achieve the convergence of the numerical solution procedure.

4. Boundary-domain integral equations

The unique advantage of the BEM originates from the application of Green fundamental solutions, e.g. $u^*(\xi,s)$ or $u^*(\xi,s;t_F,t)$, as particular weighting functions. Since they only consider the linear transport phenomenon, an appropriate selection of a linear differential operator $\mathscr{L}[\cdot]$ is of main importance in establishing a stable and accurate singular integral representations corresponding to original differential conservation equations.

All different conservation models can be written in the following general differential form:

$$\mathscr{L}[u(\cdot)]+b(\cdot)=0, \tag{18}$$

where the differential operator $\mathscr{L}[\cdot]$ can be either elliptic time non-dependent or parabolic time dependent, $u(r_j,t)$ is an arbitrary field function, and the non-homogenous term $b(r_j,t)$ is applied for nonlinear transport effects or pseudo-body forces.

When solving time dependent problems using elliptic time non-dependent fundamental solution $u^*(\xi,s)$, the field function local time derivative, e.g. $\partial u(s,t)/\partial t$, have to be approximated in various ways. The finite difference approximative numerical model is usually applied on time axis, such as the following non-symmetric first order two-time level Euler implicit scheme

$$\frac{\partial u(s,t_F)}{\partial t}\approx\frac{u(s,t_F)-u(s,t_{F-1})}{\tau}, \tag{19}$$

where a time increment $\tau=t_F-t_{F-1}$. To increase the computation accuracy at the further time steps, the three-time level second order asymmetric difference formulae can be applied

$$\frac{\partial u(s,t_F)}{\partial t}\approx\frac{3u(s,t_F)-4u(s,t_{F-1})+u(s,t_{F-2})}{2\tau}. \tag{20}$$

Above finite difference schemes can be formulated in a general form

$$\frac{\partial u(s,t_F)}{\partial t}\approx Au(s,t_F)-Bu(s,t_{F-1})+Cu(s,t_{F-2}), \tag{21}$$

where $A=1/\tau$ or $A=3/2\tau$ for the first and second scheme, respectively, etc.

4.1. Integral representations for flow kinematics

The velocity equation (13) can be recognized as a non-homogenous elliptic vector Poisson equation, thus by employing the linear elliptic Laplace differential operator

$$\mathscr{L}[\cdot]=\frac{\partial^2(\cdot)}{\partial x_j \partial x_j} \tag{22}$$

the following can be stated:

$$\mathscr{L}[v_i]+b_i=\frac{\partial^2 v_i}{\partial x_j \partial x_j}+b_i=0. \tag{23}$$

The singular boundary integral representation for the velocity vector can be formulated by using the Green theorems for scalar functions, or weighting residuals technique, rendering the following vector integral formulation, e.g. for plane flow situation

$$\begin{aligned} c(\xi)v_i(\xi)+\int_\Gamma v_i\frac{\partial u^\star}{\partial n}\,\mathrm{d}\Gamma = &\int_\Gamma \frac{\partial v_i}{\partial n}u^\star\,\mathrm{d}\Gamma+e_{ij}\int_\Gamma \omega n_j u^\star\,\mathrm{d}\Gamma \\ &-e_{ij}\int_\Omega \omega\frac{\partial u^\star}{\partial x_j}\,\mathrm{d}\Omega-\int_\Gamma \mathscr{D}n_i u^\star\,\mathrm{d}\Gamma \\ &+\int_\Omega \mathscr{D}q_i^\star\,\mathrm{d}\Omega, \end{aligned} \tag{24}$$

with $u^\star(\xi,s)$ the elliptic Laplace fundamental solution, e.g. the solution of singularly forced Laplace's equation

$$\mathscr{L}[u^*(\xi,s)]+\delta(\xi,s)=\frac{\partial^2 u^*(\xi,s)}{\partial x_i(s)\partial x_i(s)}+\delta(\xi,s)=0\,, \tag{25}$$

and is given by the logarithmic potential

$$u^*(\xi,s)=\frac{1}{2\pi}\ln\left(\frac{1}{r(\xi,s)}\right), \tag{26}$$

for the two-dimensional plane geometry.

One of the most important issues in numerical modelling of flow phenomena is to satisfy the compatibility and restriction conditions for the velocity, vorticity and local expansion fields. In case of Eq. (13), it can be easily shown that in general mass and vorticity conservation is not preserved. Thus, Eq. (24) does not in general represent the kinematics of the general fluid flow.

Applying kinematics restriction given by the statement

$$\frac{\partial v_i}{\partial n}+e_{ij}\omega n_j-\mathscr{D}n_i=-e_{ij}\frac{\partial v_j}{\partial t}, \tag{27}$$

the singular boundary-domain integral representation for the velocity vector can be formulated as, e.g. the plane two-dimensional kinematics is given by two scalar equations as follows:

$$c(\xi)v_i(\xi)+\int_\Gamma v_i q^\star\,\mathrm{d}\Gamma=e_{ij}\int_\Gamma v_j q_t^\star\,\mathrm{d}\Gamma-e_{ij}\int_\Omega \omega q_j^\star\,\mathrm{d}\Omega+\int_\Omega \mathscr{D}q_i^\star\,\mathrm{d}\Omega, \tag{28}$$

or in the form of integral vector formulation for the general flow situation

$$c(\xi)\vec{v}(\xi)+\int_\Gamma \vec{v}q^\star\,\mathrm{d}\Gamma=\int_\Gamma(\vec{q}^\star\times\vec{n})\times\vec{v}\,\mathrm{d}\Gamma+\int_\Omega\vec{\omega}\times\vec{q}^\star\,\mathrm{d}\Omega+\int_\Omega\mathscr{D}\vec{q}^\star\,\mathrm{d}\Omega. \tag{29}$$

4.2. Integral representations of pressure equation

The pressure equation (15) is an elliptic Poisson equation, and therefore employing again the linear elliptic Laplace differential operator the following form of the pressure integral equation is obtained:

$$c(\xi)p(\xi)+\int_\Gamma pq^\star\,\mathrm{d}\Gamma=\int_\Gamma\frac{\partial p}{\partial n}u^\star\,\mathrm{d}\Gamma-\int_\Gamma f_{pi}n_iu^\star\,\mathrm{d}\Gamma+\int_\Omega f_{pi}q_i^\star\,\mathrm{d}\Omega, \tag{30}$$

and, because $\partial p/\partial n=\vec{f}_p\cdot\vec{n}$, the final form of the pressure integral equation is obtained

$$c(\xi)p(\xi)+\int_\Gamma pq^\star\,\mathrm{d}\Gamma=\int_\Omega f_{pi}q_i^\star\,\mathrm{d}\Omega, \tag{31}$$

where the vector $\vec{f}_p$ is given by Eq. (16).

4.3. Integral representations for flow kinetics

Considering the vorticity or thermal heat transport in an integral representation one has to take into account parabolic diffusion convection character of the governing transport equations. With the use of the linear elliptic diffusion convection differential operator,

$$\mathscr{L}[u(\cdot)]+b(\cdot)=a_0\frac{\partial^2u}{\partial x_j\partial x_j}-\frac{\partial v_{0j}u}{\partial x_j}-\mathscr{K}_0u+b=0, \tag{32}$$

where $\mathscr{K}_0=A$ (Eq. (21)), and the velocity field $\vec{v}$ is decomposed into a homogeneous field $\vec{v}_0$ and variable part $\widetilde{\vec{v}}$, e.g.

$$\vec{v}(\vec{r})=\vec{v}_0+\widetilde{\vec{v}}(\vec{r}). \tag{33}$$

Therefore, applying the standard procedure the following boundary-domain integral representation, e.g. equivalent to Eq. (14), can be derived:

$$\begin{aligned}c(\xi)\omega(\xi,t_F)+\int_\Gamma\omega Q^\star\,\mathrm{d}\Gamma=&\frac{1}{\eta_0}\int_\Gamma\left(\eta_0\frac{\partial\omega}{\partial n}-\rho_0v_n\omega+\rho g_t+f_t^m\right)U^\star\,\mathrm{d}\Gamma\\&+\frac{1}{\eta_0}\int_\Omega(\rho_0\widetilde{v}_j\omega+\rho e_{ij}g_i+e_{ij}f_i^m)Q_j^\star\,\mathrm{d}\Omega\\&+\beta_1\int_\Omega u(s,t_{F-1})U^*(\xi,s)\,\mathrm{d}\Omega\\&-\beta_2\int_\Omega u(s,t_{F-2})U^*(\xi,s)\,\mathrm{d}\Omega,\end{aligned} \tag{34}$$

where $\beta_1=B/a,\beta_2=C/a,U^\star=a_o\,u^\star=(k_0/c_0)u^\star$, and where v_n,g_t and f_t^m are the normal velocity, and the tangential gravity and nonlinear material source components, respectively, e.g. $v_n=\vec{v}\cdot\vec{n},g_t=\vec{g}\cdot\vec{t}=-e_{ij}g_in_j$ and $f_t^m=\vec{f}^m\cdot\vec{t}=-e_{ij}f_i^mn_j$.

The free-space Green's function $u^\star(\xi,s)$ of elliptic diffusion–convection equation for an isotropic homogeneous diffusive–convective medium with uniform diffusivity a_0 and constant velocity field $\vec{v}_0$ is the solution of singularly forced adjoint equation, e.g.

$$\mathscr{L}^\star[u^\star(\xi,s)]=a_0\frac{\partial^2u^\star(\xi,s)}{\partial x_j(s)\partial x_j(s)}+\frac{\partial v_{0j}u^\star(\xi,s)}{\partial x_j(s)}-\mathscr{K}_0u^\star(\xi,s)=-\delta(\xi,s) \tag{35}$$

and is given by the expression

$$u^\star(\xi,s)=\frac{1}{2\pi a_0}K_0(\mu r)\exp\left(\frac{v_{0j}r_j}{2a_0}\right), \tag{36}$$

where K_0 is the modified Bessel function of the second kind of order 0 and the parameter μ is defined as

$$\mu^2=\left(\frac{v_0}{2a_0}\right)^2+\frac{\mathscr{K}_0}{2a_0}, \tag{37}$$

with r the modulus of $\vec{r}$, and $v_0^2=v_{0j}v_{0j}$.

The integral representation of the nonlinear heat energy transport equation is derived considering the linear elliptic diffusion–convection differential operator, therefore the following integral representation for the thermal energy kinetics, in analogy to Eq. (34), can be evaluated

$$\begin{aligned}c(\xi)T(\xi,t_F)+&\int_\Gamma TQ^\star\,\mathrm{d}\Gamma\\=&\frac{1}{k_0}\int_\Gamma\left(k\frac{\partial T}{\partial n}-cv_nT+\lambda\frac{\partial q_n}{\partial t}\right)U^\star\,\mathrm{d}\Gamma\\&-\frac{1}{k_0}\int_\Omega\left(\widetilde{k}\frac{\partial T}{\partial x_j}-c\widetilde{v}_jT-\lambda\frac{\partial q_j}{\partial t}\right)Q_j^\star\,\mathrm{d}\Omega\\&+\frac{1}{k_0}\int_\Omega\left(Tv_j\frac{\partial c}{\partial x_j}+cT\mathscr{D}-\widetilde{c}\frac{\partial T}{\partial t}+\beta T\frac{\mathrm{D}p}{\mathrm{D}t}+\Phi\right)U^\star\,\mathrm{d}\Omega\\&+\beta_1\int_\Omega u(s,t_{F-1})U^*(\xi,s)\,\mathrm{d}\Omega\\&-\beta_2\int_\Omega u(s,t_{F-2})U^*(\xi,s)\,\mathrm{d}\Omega.\end{aligned} \tag{38}$$

5. Numerical algorithm

The nonlinear system of partial differential equation described in the previous section is solved by a combination of two BEM techniques. The wavelet compressed BEM [24] is used to calculated boundary values of vorticity and pressure, while a macro-element BEM governed by a square system matrix is used to solve other equations. The algorithm is presented in detail below:

- calculate integrals, that depend solely on the mesh geometry
- use wavelet compression on matrices of integrals
- begin time step loop
  - ○ begin global nonlinear loop
    - begin local kinematic-vorticity loop
      - *KINEMATICS*
      - * calculate boundary values by solving the kinematics equation by wavelet compressed single domain BEM (Eq. (29))
      - * calculate domain velocity values by solving the kinematics equation by subdomain BEM (Eq. (24))
      - *VORTICITY KINETICS*
      - * solve vorticity transport equation by subdomain BEM using the boundary values from single domain BEM calculation
      - * check convergence—repeat steps in the local loop until convergence is achieved
    - end local kinematic-vorticity loop
    - *ENERGY KINETICS*
    - * temperature (Eq. (38))
    - *PRESSURE COMPUTATION*
    - * calculate boundary values by solving the pressure equation by wavelet compressed single domain BEM (Eq. (31))
    - * calculate domain pressure values by solving the pressure equation by subdomain BEM (Eq. (30))

- *NON-LINEAR EFFECTS*
  - * calculate all nonlinear terms (dilatation, reversible and irreversible rate of work, nonlinear material properties, non-linear heat flux model)
  - * check convergence—repeat steps in the nonlinear loop until convergence is achieved
- ○ end global nonlinear loop
- • end time step
- • output results

5.1. Solution of the kinematics equation for boundary values by wavelet compressed BEM

In order to obtain a discrete solution of the kinematics equation written in a form without derivatives of the velocity and vorticity fields (29), the boundary Γ is divided into E boundary elements Γ_e and the domain Ω is divided into C domain cells Ω_c with $\Gamma \approx \sum_{e=1}^{E}\Gamma_e$ and $\Omega \approx \sum_{c=1}^{C}\Omega_c$. Within each boundary element and each internal cell the field functions are approximated by boundary φ_i^b and domain φ_i^d shape functions $\vec{v} = \sum_{i=1}^{n_b}\vec{v}^i\varphi_i^b$, $\vec{\omega} = \sum_{i=1}^{n_d}\vec{\omega}^i\varphi_i^d$ and $\mathscr{D} = \sum_{i=1}^{n_d}\mathscr{D}^i\varphi_i^d$, where n_b and n_d are the number of nodes in a boundary element and in a domain cell. In this paper we used three node quadratic boundary elements and nine node Lagrange domain cells. Inserting approximations into Eq. (29) we have

$$\begin{aligned} c(\xi)\vec{v}(\xi) + \sum_{e=1}^{E}\sum_{i=1}^{n_b}\vec{v}^i\left(\int_{\Gamma_e}\varphi_i^b q^\star \,\mathrm{d}\Gamma\right) &= \sum_{e=1}^{E}\sum_{i=1}^{n_b}\vec{v}^i \times \left(\int_{\Gamma_e}\varphi_i^b(\vec{n}\times\vec{q}^\star)\,\mathrm{d}\Gamma\right) \\ &+ \sum_{c=1}^{C}\sum_{i=1}^{n_d}\vec{\omega}^i \times \left(\int_{\Omega_c}\varphi_i^d\vec{q}^\star\,\mathrm{d}\Omega\right) \\ &+ \sum_{c=1}^{C}\sum_{i=1}^{n_d}\mathscr{D}^i\left(\int_{\Omega_c}\varphi_i^d\vec{q}^\star\,\mathrm{d}\Omega\right). \end{aligned} \tag{39}$$

There are three types of integrals in the above equation. In all, the integrand is a derivative of the fundamental solution multiplied by the shape function and the unit normal. The values of integrals depend solely on the mesh and the shape functions chosen, thus they can be calculated before starting the nonlinear iterative procedure. The integrals are traditionally named as $h_{i,e}$, $\vec{h}_{i,e}^{\,t}$ and $\vec{d}_{i,c}$, respectively. In order to obtain a non-singular system of equations for boundary vorticities from Eq. (39), one must use its tangential form [26], obtained by taking a cross product of Eq. (39) with the unit normal in the source point:

$$\begin{aligned} c(\xi)\vec{n}(\xi)\times\vec{v}(\xi) + \vec{n}(\xi)\times\sum_{e=1}^{E}\sum_{i=1}^{n_b}\vec{v}^i h_{i,e} &= \vec{n}(\xi)\times\sum_{e=1}^{E}\sum_{i=1}^{n_b}\vec{v}^i\times\vec{h}_{i,e}^{\,t} \\ &+ \vec{n}(\xi)\times\sum_{c=1}^{C}\sum_{i=1}^{n_d}\vec{\omega}^i\times\vec{d}_{i,c} \\ &+ \vec{n}(\xi)\times\sum_{c=1}^{C}\sum_{i=1}^{n_d}\mathscr{D}^i\vec{d}_{i,c}. \end{aligned} \tag{40}$$

We now define the planar geometry. The fluid flows in the x–y plane, vorticity has only one non-zero component in the z direction. Since we are dealing with velocity on the boundary, it is convenient to introduce normal velocity $v_n = n_x v_x + n_y v_y$ and tangential velocity $v_t = n_x v_y - n_y v_x$ and treat vorticity as a scalar quantity $\vec{\omega} \to \omega_z = \omega$. The integral vector $\vec{h}^t$ has also only one non-zero component and will be also treated as scalar h^t. When the cross products of Eq. (40) are calculated and the system of equations is simplified to planar geometry, we obtain a non-zero equation in z direction only:

$$\begin{aligned} c(\xi)v_t(\xi) + \sum_{e=1}^{E}\sum_{i=1}^{n_b}v_t^i h_{i,e} = &-\sum_{e=1}^{E}\sum_{i=1}^{n_b}v_n^i h_{i,e}^t \\ &+ \sum_{c=1}^{C}\sum_{i=1}^{n_d}\omega^i(n_x d_{i,c}^x + n_y d_{i,c}^y) \\ &+ \sum_{c=1}^{C}\sum_{i=1}^{n_d}\mathscr{D}^i(n_x d_{i,c}^y - n_y d_{i,c}^x). \end{aligned} \tag{41}$$

The source point ξ is set in all boundary nodes in order to obtain a system of linear equations. The field function values in nodes are represented by vectors $v_t^i \to \{v_t\}, v_n^i \to \{v_n\}$. The vorticity is divided into a boundary vector $\omega_{i\in\Gamma}^i \to \{\omega^\Gamma\}$ and a domain vector $\omega_{i\in\Omega\setminus\Gamma}^i \to \{\omega^{\Omega\setminus\Gamma}\}$. The dilatation field is assembled into a vector in a similar manner $\mathscr{D}^i \to \{\mathscr{D}\}$. The integrals are assembled into matrices accordingly. With the boundary vorticities as unknowns, the matrix–vector form of Eq. (41) is

$$[D^\Gamma]\{\omega^\Gamma\} = ([C]+[H])\{v_t\} + [H^t]\{v_n\} - [D^{\Omega\setminus\Gamma}]\{\omega^{\Omega\setminus\Gamma}\} - [D]\{\mathscr{D}\}. \tag{42}$$

The matrices $[D^\Gamma], [C], [H]$ and $[H^t]$ are square, fully populated and unsymmetrical with the number of boundary nodes of rows and columns. Although full, the storage requirements for these matrices are not large, since the number of boundary nodes is very small compared to the number of domain nodes. On the other hand, the matrix $[D^{\Omega\setminus\Gamma}]$ is rectangular and also full and unsymmetrical and has dimensions of the number of boundary nodes rows and the number of domain nodes columns. The reason that the $[D^{\Omega\setminus\Gamma}]$ scales with the number of domain nodes is the fact that a fundamental solution of a Poisson type of equation does not exist and that we had to use the Laplace fundamental solution. This yielded a domain integral in the integral representation, which requires discretization of the domain and ultimately the storage of a matrix that scales with the number of nodes in the domain. Storing this matrix in memory requires huge amount of on-board memory and thus limits the size of meshes that can be used. To tackle this problem we employed a wavelet transform technique for rectangular matrices developed by Ravnik et al. [24]. The transform is based on Haar wavelets and the fast wavelet transform algorithm of Beylkin [27]. The technique has already been successfully used for a planar LES of turbulent natural convection by Ravnik et al. [25].

In order to reduce the storage and CPU time requirements we will calculate the matrix vector product $[D^{\Omega\setminus\Gamma}]\{\omega^{\Omega\setminus\Gamma}\}$ using a wavelet compressed matrix of integrals. Since we will compress only the domain matrix, we will change only right-hand side of our system of equations, leaving the system matrix unperturbed. By introducing an error estimation algorithm, we will be able to keep the error of right-hand side calculation of the same order than the error of the solution of the system.

Let W be a wavelet transform matrix, which transforms a vector to a wavelet basis. It is set up using the Haar wavelet transform for vectors of arbitrary length [24] and is capable of transforming matrices of arbitrary size. The W transform is still in its essence the Haar wavelet transform. Before the Haar transformation, the vector is modified in such manner, that just the right number of wavelet coefficient end up zero. Not storing zeros makes it possible to apply the W transform to a vector with an arbitrary number of components and store only the same number of wavelet coefficients.

Since the product of wavelet matrix W and its transpose W^{T} is an identity, we may write

$$[D^{\Omega\setminus\Gamma}]\{\omega^{\Omega\setminus\Gamma}\} = W^{\mathrm{T}}(\underbrace{W[D^{\Omega\setminus\Gamma}]W^{\mathrm{T}}}_{[D_W^{\Omega\setminus\Gamma}]}W\{\omega^{\Omega\setminus\Gamma}\}). \tag{43}$$

The wavelet compressed matrix of integrals $[D_W^{\Omega\setminus\Gamma}] = W[D^{\Omega\setminus\Gamma}]W^{\mathrm{T}}$ is the wavelet transform of all rows and columns of the original matrix of integrals $[D^{\Omega\setminus\Gamma}]$. Small (in absolute sense) elements of matrix $[D_W^{\Omega\setminus\Gamma}]$ may be zeroed without diminishing the accuracy of the matrix vector product in Eq. (43). Wavelet compression is preformed only once, prior to the iterative process. The matrices W and W^{T} are not actually stored in memory, but are rather calculated on the fly, thus omitting the need of additional storage. During the compression process we measure relative difference between full matrix times random vector product and compressed matrix times the same vector. The compression is stopped, when the relative difference reaches a prescribed criteria ε. In our previous work [25], we have determined that using compression with $\varepsilon = 10^{-5}$ has virtually no influence on the accuracy of the flow simulation. The resulting sparse matrix is written in compressed row storage format to save computer memory. In each iteration we must instead of one full matrix time vector product perform a wavelet transform of the domain vorticity values $W\{\omega^{\Omega\setminus\Gamma}\}$, a sparse matrix times vector product $[D_W^{\Omega\setminus\Gamma}]W\{\omega^{\Omega\setminus\Gamma}\}$ and an inverse wavelet transform $W^{\mathrm{T}}([D_W^{\Omega\setminus\Gamma}]W\{\omega^{\Omega\setminus\Gamma}\})$. All our tests showed that full matrix time vector product requires more CPU time, thus wavelet compression saves storage and CPU time. However, since the matrix times vector product (43) presents only a small fraction of the total CPU time requirements, the decrease of CPU time is almost negligible. On the other hand, the decrease of storage requirements is substantial and enables high density meshes to be used with our algorithm. In the same manner, the product $[D]\{\mathscr{D}\}$ can be compressed as well.

The final wavelet BEM based discrete form of the kinematics equation for the calculation of boundary vorticity values is

$$[D^{\Gamma}]\{\omega^{\Gamma}\} = ([C]+[H])\{v_t\} + [H^t]\{v_n\} - W^{\mathrm{T}}([D_W^{\Omega\setminus\Gamma}]W\{\omega^{\Omega\setminus\Gamma}\}) - W^{\mathrm{T}}([D_W]W\{\mathscr{D}\}). \quad (44)$$

Since the system matrix $[D^{\Gamma}]$ depends on the mesh geometry only and is constant throughout the simulation, the solution of the system is obtained using a direct solver with LU decomposition.

5.2. Macro-element BEM

With the aim of decreasing storage and CPU time requirements of the single domain BEM we employ the macro-element approach. The idea is to use a collocation scheme for equation for each domain cell separately and require that the functions must be continuous over the domain cell boundaries. Since every domain cell neighbours only to a few cells, we end up with a sparse system of equations. In a nutshell we are using single domain BEM on every domain cell separately and connect them via compatibility and equilibrium conditions [26].

6. Numerical example

Using the developed numerical scheme we analysed the onset of thermoacoustic waves in an enclosure. The enclosure is 13 mm wide and 13 mm high. It is filled with nitrogen gas at $p = 101\,325$ Pa and $T_0 = 300$ K. In the beginning the fluid is at rest. At $t = 0$ the left wall is impulsively heated to $T_L = 400$ K. During the simulation ($t > 0$) a constant temperature of $T_R = 300$ K is kept on the right wall and $T_L = 400$ K on the left. The top and bottom walls of the enclosure are considered adiabatic, i.e. there is no heat flux through them. Gravity is neglected. The enclosure is closed by walls, which have a no-slip velocity boundary condition. The enclosure and boundary conditions are shown in Fig. 1.

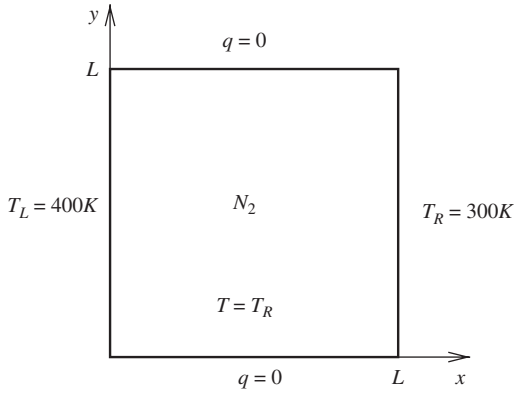

Fig. 1. Geometry and boundary conditions of the problem ($L = 0.013$ m).

The ideal gas is chosen as a working fluid, thus the equation of state for the perfect gas is applied

$$p = \rho R T, \quad (45)$$

to relate the temperature to the other thermodynamic quantities. In the present research the Prandtl (Pr) number is assumed to remain constant, e.g. the following constant physical values are selected for the nitrogen (N_2): $\kappa = 1.4, R = 296.7$ and $Pr = 0.713$. The temperature dependence of the material properties is taken into account using the following polynomial expressions, e.g. for the dynamic viscosity η:

$$\eta(T) = -1.253\times10^{-6} + 8.983\times10^{-8}T - 1.139\times10^{-10}T^2 + 9.101\times10^{-14}T^3, \quad (46)$$

the heat conductivity

$$k(T) = 1.494\times10^{-4} + 1.108\times10^{-4}T - 1.045\times10^{-7}T^2 + 6.958\times10^{-11}T^3, \quad (47)$$

while the heat relaxation time value $\lambda = 0.1$ was selected. The influence of temperature on c_p is neglected.

For the impulsive heating, the temperature of the left wall is given as

$$T_L(t) = T_0(1+A), \quad (48)$$

where the over heat ratio A is given by an expression

$$A = \frac{T_L - T_0}{T_0}, \quad (49)$$

and $A = \frac{1}{3}$ for all cases presented for spatially uniform wall heating, thus the left wall temperature is equated to $T_L = 400$ K.

Three meshes were used in simulations. The coarse mesh with 20×20 elements (1681 nodes), the middle mesh with 30×30 elements (3721 nodes) and the fine mesh with 40×40 elements (6561 nodes). A geometrical series was used to determine the size of elements. The ratio between the largest element in the middle of the enclosure and the smallest elements on the boundary was 2.

Two time steps were used for simulation. The long time step of $\Delta t = 10^{-4}$ s, which enabled a long-term simulation reaching steady state. The short time step of $\Delta t = 10^{-6}$ s enabled an insight into the physics of the phenomenon. The short time step was used on the coarse and middle meshes, while the long time step was employed on the fine mesh.

The short time step simulation lasted for 0.8 s. In Figs. 2 and 3 we are showing the temperature field and the velocity fields at $t = 0.15$ s. We observe that the diffusion carried the temperature

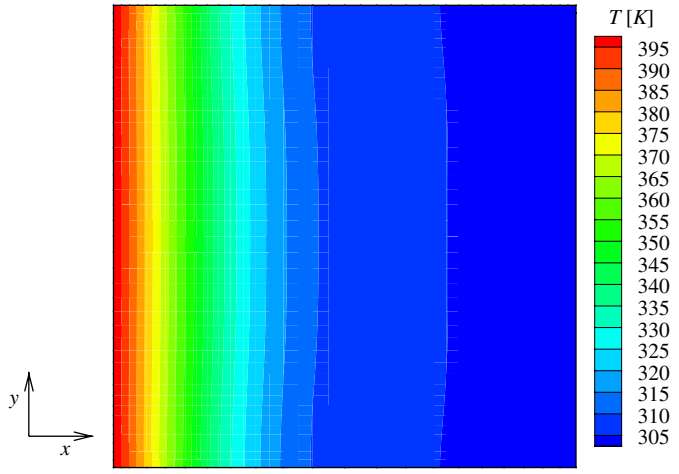

Fig. 2. Temperature contours at $t = 0.15$ s, zero gravity condition, 20×20 element mesh, $\Delta t = 10^{-4}$ s.

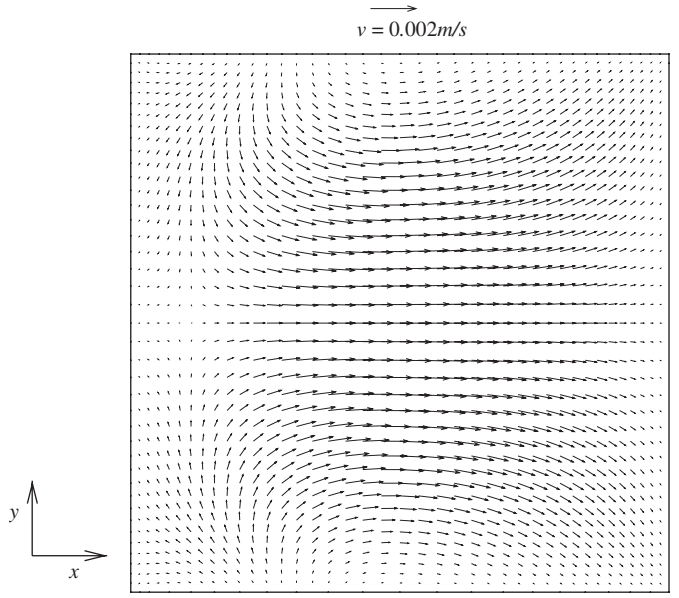

Fig. 3. Velocity vectors at $t = 0.15$ s, zero gravity condition, 20×20 element mesh, $\Delta t = 10^{-4}$ s.

field approximately halfway into the cavity. Since there is no gravity and hence no buoyancy the flow field appears to be one-dimensional. The velocity field is weakening with time.

A point in the middle of the enclosure ($x = 0.065$ m, $y = 0.065$ m) was chosen for demonstration of the time development of the flow. In Fig. 4 a pressure evolution with time is shown. We observe a gradual increase of pressure, faster in the first tenth of a second and slower after that. No pressure waves are observed, which was expected since the time step is too long to capture phenomena which occur with the speed of sound. The pressure distribution in the enclosure is uniform. At $t = 0.8$ s the pressure reaches about $p = 114\,000$ Pa. Fig. 5 compares pressure versus time graphs for meshes with 20×20 and 30×30 elements. Since the results are virtually identical, we present all other short time step results on the coarse mesh.

Looking at the evolution of the temperature of nitrogen in the middle of the enclosure in Fig. 6 we observe that the temperature

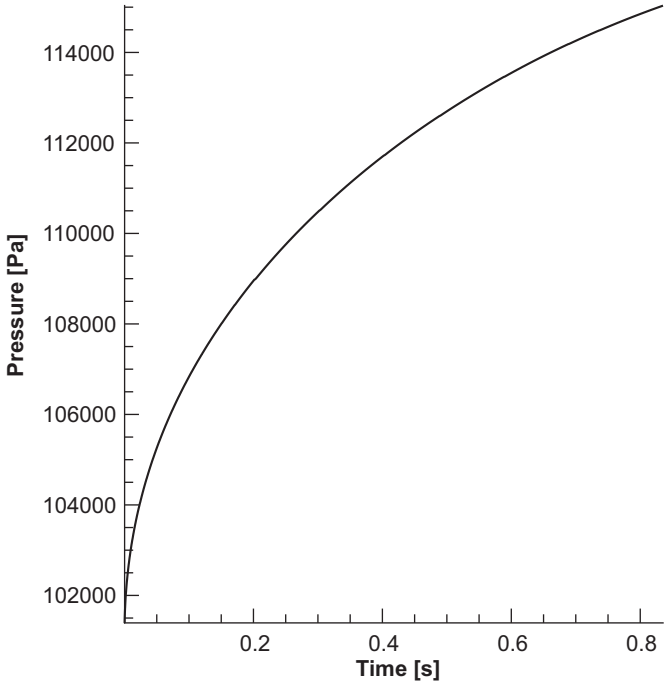

Fig. 4. Pressure in the centre of the enclosure ($x = 0.065$ m, $y = 0.065$ m) versus time.

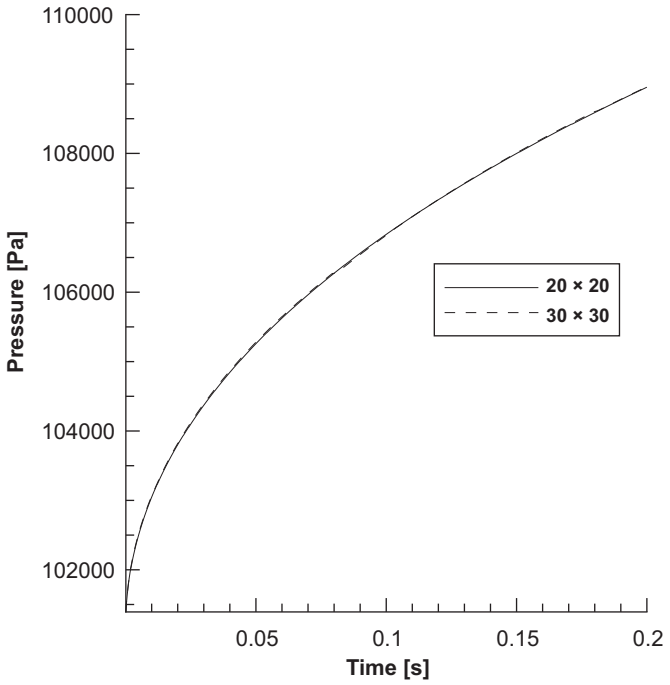

Fig. 5. Comparison of pressure versus time graphs on 20×20 and 30×30 element meshes.

increase is more or less linear. The nitrogen in the centre of the enclosure reaches $T = 340$ K.

Fig. 7 shows the evolution of heat flux through the left wall. Extremely high values $dT/dn \approx 10^5$ K/m are found in the beginning of the simulation, which are caused by impulsive heating at $t = 0$. After the diffusive process starts, the flux decreases and remains approximately constant throughout the simulation.

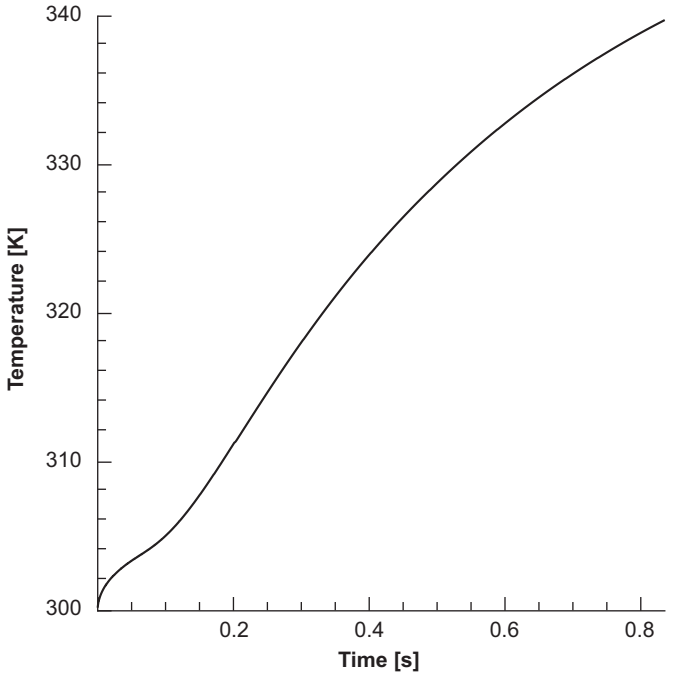

Fig. 6. Temperature in the centre of the enclosure ($x = 0.065\,\text{m}, y = 0.065\,\text{m}$) versus time. A more or less constant increase of temperature with time is observed; 20×20 element mesh, $\Delta t = 10^{-4}$ s.

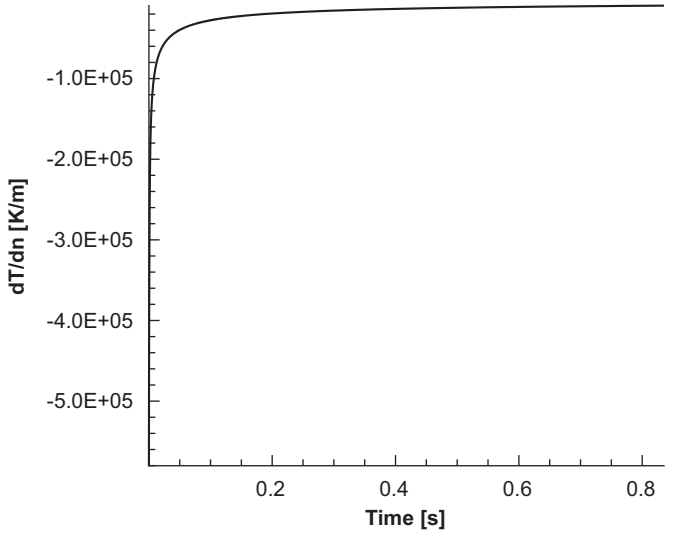

Fig. 7. Temperature flux in the centre of the left wall ($x = 0, y = 0.065\,\text{m}$) versus time. A very high flux is simulated at the beginning of the simulation; 20×20 element mesh, $\Delta t = 10^{-4}$ s.

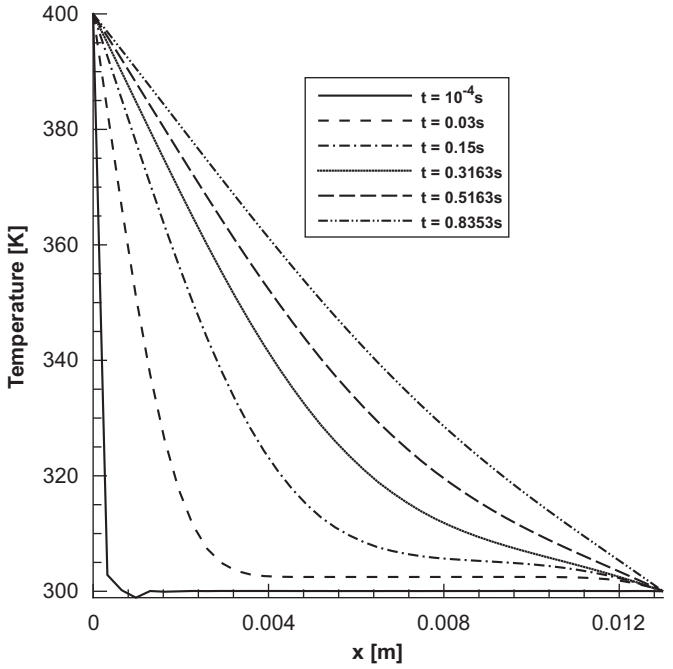

Fig. 8. Temperature profiles through the centreline of the cavity. Development of the profile with time can be seen; 20×20 element mesh, $\Delta t = 10^{-4}$ s.

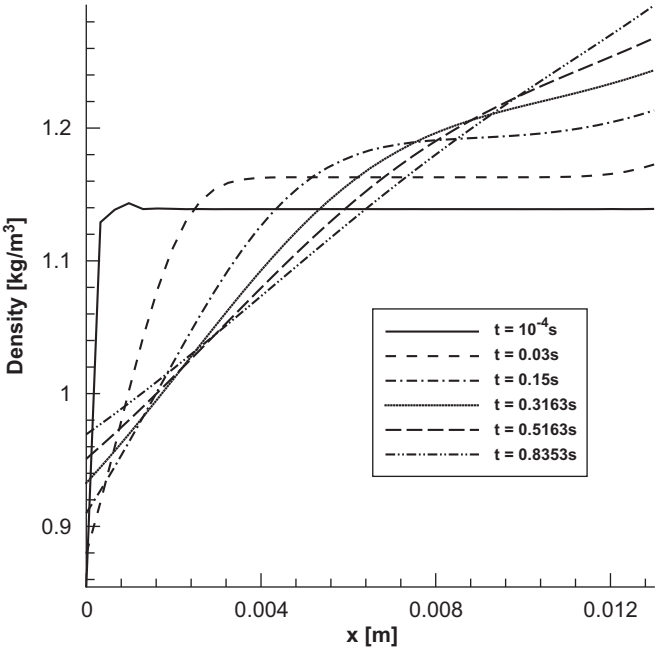

Fig. 9. Density profiles through the centreline of the cavity. Development of the profile with time can be seen; 20×20 element mesh, $\Delta t = 10^{-4}$ s.

To show the variation of flow fields across the enclosure we examined profiles along the horizontal centreline $(x, 0.065\,\text{m})$. Fig. 8 shows temperature profiles for six time instants. The very sharp temperature profile in the beginning of the simulation is caused by the application of boundary conditions. At long times, a steady state diffusive temperature profile is observed. Since the ideal gas approximation of nitrogen is assumed and since the pressure distribution in the cavity is uniform the density profiles are reciprocal to those of temperature (Fig. 9). The profiles of the horizontal component of velocity are shown in Fig. 10 for several time instants. We observe a diminishing velocity field with time. At $t = 0.8$ s nitrogen is reaching velocities of the order of 10^{-5} m/s.

The simulation on the fine mesh was performed using a time step of 10^{-6} s. The velocity field is visualized using vectors in Fig. 11. Alternating sign of the horizontal velocity component, which characterizes the travelling pressure wave, is clearly visible.

Fig. 12 shows the time evolution of pressure and horizontal velocity component in the centre of the enclosure. Due to the presence of thermoacoustic waves a fluctuating increase of

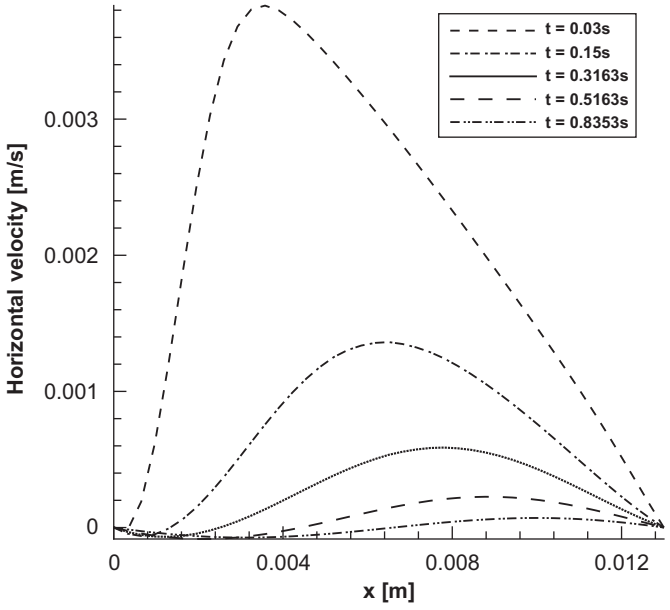

Fig. 10. Horizontal velocity profiles through the centreline of the cavity. After the initial high velocity the velocity field settles down with time; 20×20 element mesh, $\Delta t = 10^{-4}$ s.

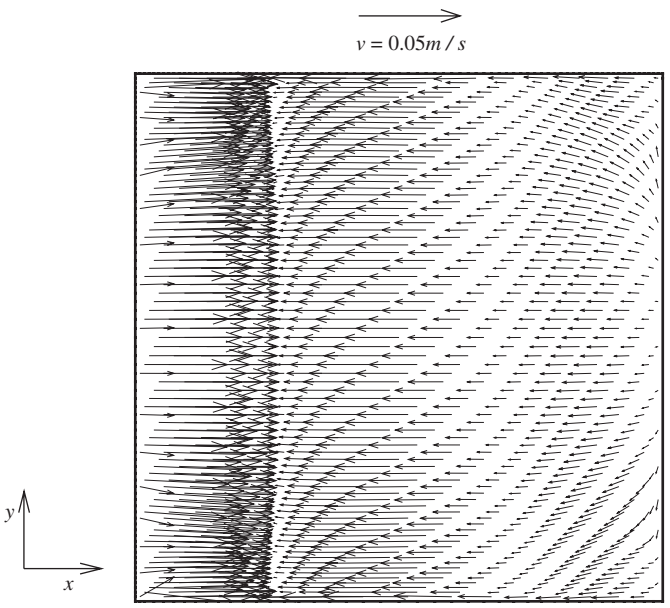

Fig. 11. Velocity vectors at a time instant $t = 10^{-4}$ s. Only every 5th vector is shown; 40×40 element mesh, $\Delta t = 10^{-6}$ s.

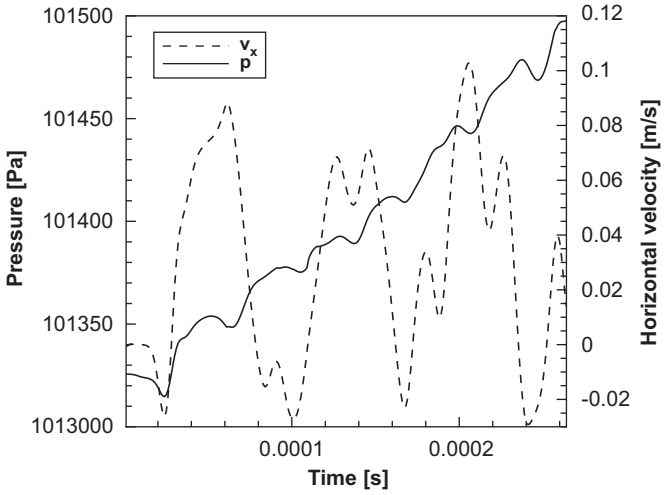

Fig. 12. Pressure and horizontal velocity in the centre of the enclosure with time; 40×40 element mesh, $\Delta t = 10^{-6}$ s. Due to the presence of thermoacoustic waves a fluctuating increase of pressure and changing sign of horizontal velocity is observed.

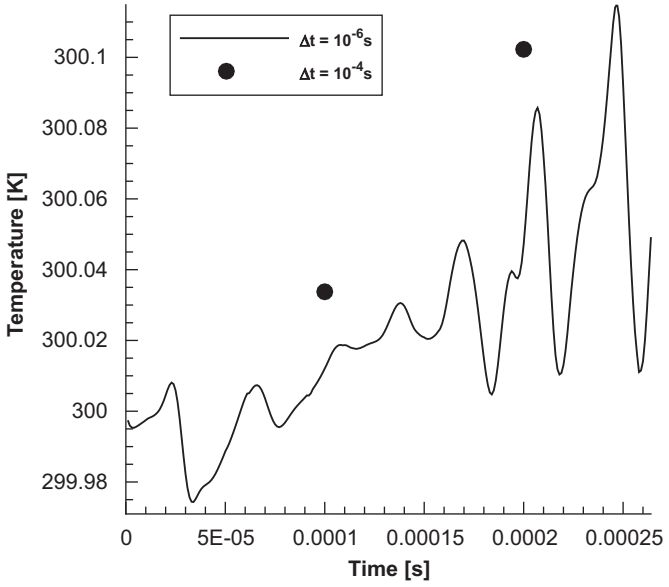

Fig. 13. Temperature in the centre of the enclosure with time; 40×40 element mesh, $\Delta t = 10^{-6}$ s. Due to the presence of thermoacoustic waves a fluctuating increase of pressure and temperature is observed.

pressure and changing sign of horizontal velocity is observed. At the same time a fluctuating increase of temperature is also observed (Fig. 13). As the pressure wave travels through the enclosure it causes local changes of temperature and density in accordance with the perfect gas law. A decrease of pressure results in a decrease of both pressure and density. The changes of temperature in the middle of the enclosure are entirely caused by this effect, since the times considered are too short for the diffusive heat transfer to reach the centre of the enclosure.

Fig. 14 shows pressure profiles across the centreline of the enclosure at $t = 10$ and 30 μs. By measuring the distance travelled by the thermoacoustic wave between these time instants we were able to estimate the speed of sound to about 322 m/s, which is within 10% of the correct value for nitrogen. This analysis was done using the first wave travelling across the enclosure from left to right. As the wave is reflected of the right wall, such analysis is no longer possible, since the waves interfere.

Fig. 15 shows the extremely high values of temperature flux at the left wall in the beginning of the simulation. As the simulation progressed we observed an approximately linear decrease of heat flux.

The non-Fourier heat transfer model was simulated on the fine mesh with a time step of $\Delta t = 10^{-6}$ s. A comparison of the evolution of pressure in the centre of the enclosure between the simulation with Fourier heat transfer model and non-Fourier heat transfer model is shown on Fig. 16. In the same manner comparison of temperature and horizontal velocity evolution in the centre of the enclosure is shown in Figs. 17 and 18.

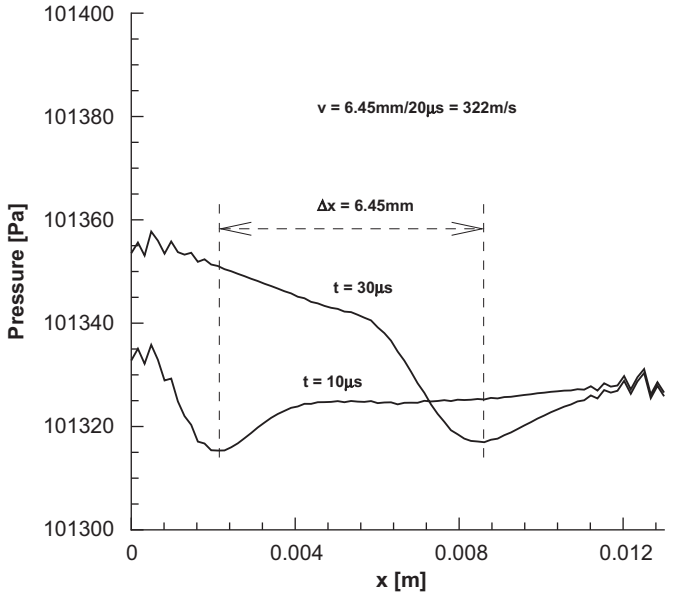

Fig. 14. Animation of pressure profiles through the centre of the enclosure; 40×40 element mesh, $\Delta t = 10^{-6}$ s. By measuring the distance travelled by the thermoacoustic wave, we were able to estimate the speed of sound to about 322 m/s.

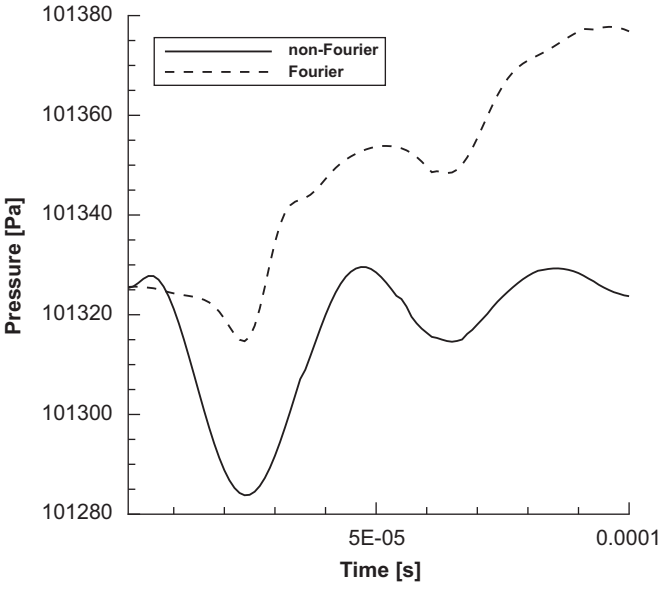

Fig. 16. Pressure in the centre of the enclosure with time; 40×40 element mesh, $\Delta t = 10^{-6}$ s. Comparison of Fourier and non-Fourier heat diffusion rheological models.

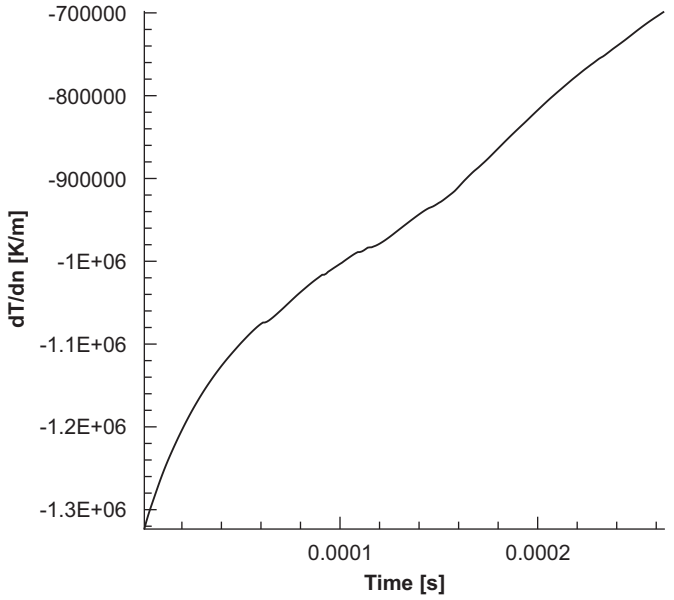

Fig. 15. Temperature flux at (0, 0.065 m) shown versus time; 40×40 element mesh, $\Delta t = 10^{-6}$ s.

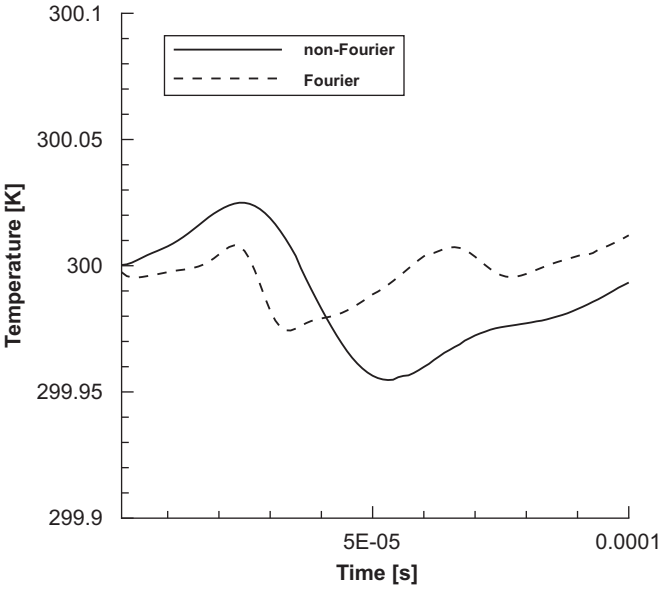

Fig. 17. Temperature in the centre of the enclosure with time; 40×40 element mesh, $\Delta t = 10^{-6}$ s. Comparison of Fourier and non-Fourier heat diffusion rheological models.

Using subsequent pressure profiles we were able to estimate the distance travelled by the pressure wave in a specified time interval. This enabled the estimation of the speed of sound, which amounted to about 318 m/s. The two profiles were selected to be 10 μs apart and are displayed in Fig. 19.

7. Conclusions

In this work a numerical algorithm for solving laminar compressible viscous flow and heat transfer was presented. The algorithm solves the velocity–vorticity formulation of Navier–Stokes equations using a combination of wavelet compressed BEM and macro-element BEM. Usage of wavelet compression and macro-element technique enables employment of higher density meshes and longer simulation times.

The method is used to simulate the onset of thermoacoustic waves in a nitrogen filled enclosure subjected to a high temperature gradient. The results show the occurrence of thermoacoustic waves travelling across the enclosure at the speed of sound. Extremely high gradients are present in the flow field, which generate the pressure waves and are difficult to model numerically. Our findings are consistent with numerical and experimental results of other authors, confirming the applicability

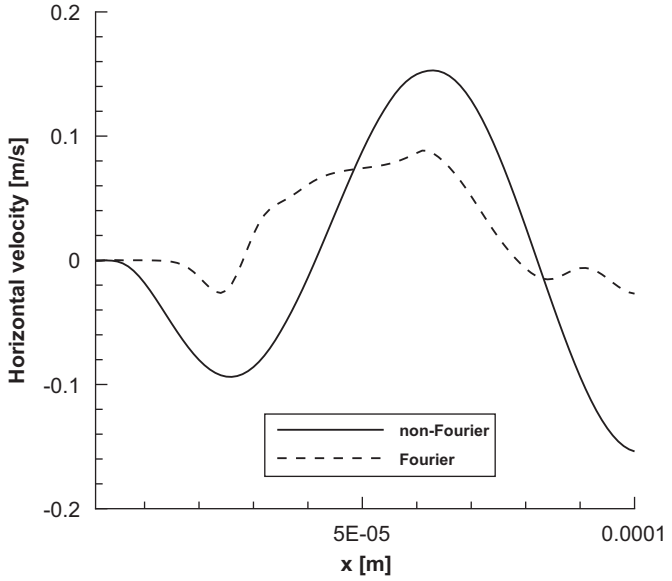

Fig. 18. Horizontal velocity in the centre of the enclosure shown with respect to time; 40×40 element mesh, $\Delta t = 10^{-6}$ s. Comparison of Fourier and non-Fourier heat diffusion rheological models.

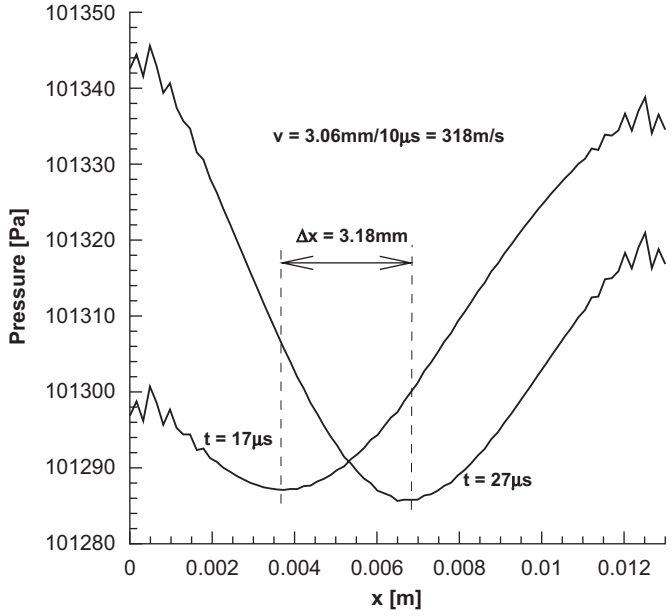

Fig. 19. Two pressure profiles, which are 10 μs apart are shown for the non-Fourier heat diffusion rheological model; 40×40 element mesh, $\Delta t = 10^{-6}$ s. Using the distance travelled by the pressure wave, we were able to estimate the speed of sound to about 318 m/s.

of BEM for such flows. In the future advanced compression and acceleration techniques, such as hierarchical matrices and ACA will be enable further reduction of complexity and thus enable simulations on meshes of higher density.

References

[1] Huang Y, Bau H. Thermoacoustic waves in a semi-infinite medium. Int J Heat Mass Transfer 1995;38:1329–45.
[2] Huang Y, Bau H. Thermoacoustic waves in a confined medium. Int J Heat Mass Transfer 1997;40:407–19.
[3] Brown M, Churchill S. Experimental measurements of pressure waves generated by impulsive heating of a surface. AIChE J 1995;41:205–13.
[4] Lin Y, Farouk B. Flows induced by thermoacoustic waves in an enclosure: effect of gravity. J Thermophys Heat Transfer 2006;20:376–83.
[5] Aktas M, Farouk B. Numerical simulation of developing natural convection in an enclosure due to rapid heating. Int J Heat Mass Transfer 2003;46: 2253–61.
[6] Farouk B, Oran ES, Brown MA. Numerical study of thermoacoustic waves in an enclosure. Phys Fluids 2000;12:1052–61.
[7] Škerget L, Ravnik J. Numerical simulation of compressible fluid flow in an enclosure induced by thermoacoustic waves. In: Simos T, editor, Numerical analysis and applied mathematics, AIP conference proceedings, vol. 936. American Institute of Physics; 2007. p. 523–6.
[8] Wu JC, Thompson J. Numerical solutions of time-dependent incompressible Navier–Stokes equations using an integro-differential formulation. Comput Fluids 1973;1:197–215.
[9] Wu JC, Rizk YM, Sankar NL. In: Problems of time-dependent Navier–Stokes flow. Developments in BEM, vol. 3. London, NY: Elsevier Applied Science Publisher; 1984 [chapter 6].
[10] Škerget L, Alujevič A, Brebbia CA, Kuhn G. In: Natural and forced convection simulation using the velocity–vorticity approach. Topics in boundary element research, vol. 5. Berlin: Springer; 1989. p. 49–86.
[11] Škerget L, Samec N. BEM for the two-dimensional plane compressible fluid dynamics. Eng Anal Boundary Elem 2005;29:41–57.
[12] Škerget L, Jecl R. In: Compressible fluid dynamics in porous media by the boundary element method. Emerging technologies and techniques in porous media—NATO science series, vol. 134. Dordrecht, Boston, London: Kluwer Academic Publishers; 2007 [chapter 6].
[13] Young DL, Liu YH, Eldho TI. A combined BEM–FEM model for velocity–vorticity formulation of the Navier–Stokes equations in three dimensions. Eng Anal Boundary Elem. 2000;24:307–14.
[14] Zhou B. Finite volume solution of the Navier–Stokes equations in velocity--vorticity formulation. Int J Numer Methods Fluids 2005;48:607–29.
[15] Wrobel LC. The boundary element method. New York: Wiley; 2002.
[16] Škerget L, Hriberšek M, Kuhn G. Computational fluid dynamics by boundary domain integral method. Int J Numer Methods Eng 1999;46: 1291–311.
[17] Ramšak M, Škerget L. A subdomain boundary element method for high-Reynolds laminar flow using stream function—vorticity formulation. Int J Numer Methods Fluids 2004;46:815–47.
[18] Ravnik J, Škerget L, Žunič Z. Combined single domain and subdomain BEM for 3D laminar viscous flow, Eng Anal Boundary Elem, in press, doi:10.1016/j.enganabound.2008.06.006.
[19] Ravnik J, Škerget L, Žunič Z. Velocity–vorticity formulation for 3D natural convection in an inclined enclosure by BEM. Int J Heat Mass Transfer 2008;51:4517–27.
[20] Hriberšek M, Škerget L. Boundary domain integral method for high Reynolds viscous fluid flows in complex planar geometries. Comput Methods Appl Mech Eng 2005;194:4196–220.
[21] Žunič Z, Hriberšek M, Škerget L, Ravnik J. 3-D boundary element-finite element method for velocity–vorticity formulation of the Navier–Stokes equations. Eng Anal Boundary Elem 2007;31:259–66.
[22] Ravnik J, Škerget L, Hriberšek M, Žunič Z. Numerical simulation of dilute particle laden flows by wavelet BEM–FEM. Comput Methods Appl Mech Eng 2008;197(6–8):789–805.
[23] Popov V, Power H, Škerget L. Domain decomposition techniques for boundary elements application to fluid flow. Southampton, Boston: WIT Press; 2007.
[24] Ravnik J, Škerget L, Hriberšek M. The wavelet transform for BEM computational fluid dynamics. Eng Anal Boundary Elem 2004;28:1303–14.
[25] Ravnik J, Škerget L, Hriberšek M. 2D velocity vorticity based LES for the solution of natural convection in a differentially heated enclosure by wavelet transform based BEM and FEM. Eng Anal Boundary Elem 2006;30: 671–86.
[26] Škerget L, Hriberšek M, Žunič Z. Natural convection flows in complex cavities by BEM. Int J Numer Methods Heat Fluid Flow 2003;13:720–35.
[27] Beylkin G, Coifman R, Rokhlin V. Fast wavelet transforms and numerical algorithms. Commun Pure Appl Math 1991;44:141–83.